Effect of Short-Time Carburizing Treatment on Microstructure and Mechanical Properties of M50 Steel

Yinghua Wei[1] · Xingfu Yu[2] · Shuai Wang[3] · Xiangyang Shen[1] · Wenzeng Zhao[2] · Yong Su[3] · Yu Yang[4] · Xiaochuan Feng[5]

Abstract

By using scanning electron microscope (SEM), transmission electron microscope (TEM), X-Ray diffraction (XRD), and hardness and rotational bending fatigue tests, the effect of short-time carburizing treatment on the microstructure and mechanical properties of bearing steel was studied. The results show that when the M50 steel is not carburized, the hardness is 750 HV, the rotational bending fatigue limit is 1100 MPa, and the impact absorption energy is 15.46 J. After short-time carburization with the carbon potential of 0.6%, the maximum hardness in the carburized area, the rotational bending fatigue limit and the impact absorption energy are all increased to be 807.7 HV, 1210 MPa and 16.72 J respectively. When the carbon potential is further enhanced to be 0.8%, the maximum hardness of the carburized area of the steel is further enhanced to be 813.4 HV, but the rotational bending fatigue strength and the impact absorption energy are both decreased to be 1125 MPa and 13.65 J respectively, which has close relations with the increasement of undissolved carbides and the precipitation of acicular carbides.

1 Introduction

M50 steel is a kind of high-temperature bearing steel with excellent comprehensive properties, which has been widely used in the aerospace field and often used as the manufacturing material for aero-engine spindle bearings [1–4]. At present, the vacuum heat treatment is mainly used of to obtain the tempered martensite-based microstructure, which has high hardness but low impact toughness. By austempering treatment of M50 steel, the mixed microstructure of martensite + bainite can be obtained, which has better performance than that of the traditional single martensite or bainite microstructure [5–7]. For bearing steel, in addition to the matrix microstructure, the quantity, morphology and distribution characteristics of carbides precipitated during heat treatment are also important factors affecting the performance of bearing steel. Therefore, reasonable allocation of carbon content and distribution is beneficial to improve the mechanical properties of bearing steel [8–10]. However, when the carbon content in the matrix is too high, the impact toughness is reduced. For some steel grades, the appropriate surface carbon content can be obtained by carburizing to improve surface hardness and wear resistance, and the toughness of the core is maintained.

Carburizing is a surface treatment process that increases the carbon content of the surface layer of the steel. The gradually decreasing carbon content changes the microstructure after heat treatment, especially in the surface layer of carburized steel. The residual compressive stress layer is formed in the surface layer through carburizing, which has positive effect on the fatigue life of the steel. Peng et al. [11] found that the fatigue limit of carburized AISI316L was 22% higher than that of the uncarburized sample, which was mainly attributed to the residual compressive stress caused

✉ Xingfu Yu
  yuxingfu@163.com

1 School of Materials Science and Engineering, Shenyang University of Technology, Shenyang 110870, China

2 School of Mechanical Engineering, Shenyang University of Technology, Shenyang 110870, China

3 School of Mechanical and Power Engineering, Shenyang University of Chemical Technology, Shenyang 110142, China

4 Key Laboratory of Power Transmission Technology on Aero-Engine, Aero Engine Corporation of China, Shenyang 110015, China

5 AECC Harbin Bearing Co., Ltd, Harbin 150500, China

by the carbon concentration distribution in the surface layer and the solid solution strengthening caused by the infiltrated carbon atoms. Studies have shown that the residual stress can be relaxed and redistributed in the carburized surface during the action of fatigue loading [12–15]. Qin et al. [16] found that the fatigue performance of 18CrNiMo7-6 steel decreases with the increase of carburizing layer depth. After carburized, the fatigue failure mode of materials is internal failure, and the residual austenite plays a major role. Su et al. [17] studied the microstructure and hardening mechanism of 15MnNi4Mo steel carburizing layer, and found that martensite and residual austenite are decomposed into carbides after carburizing treatment. The hardness of carburizing layer can be improved by refining martensite lath, reducing residual austenite content and increasing dislocation density. Li et al. [18] studied the effect of carburizing treatment on the microstructure of Fe-Cr-2Ni-Mo-V steel, and found that the gradient of martensite microstructure from surface to core was related to carbon content, with a large amount of residual austenite in the surface and basically no residual austenite in the core. For high carbon steel, such as GCr15 steel, some scholars have improved surface carbon content by carburizing to reduce surface Ms point. During the austempering process, the surface carburized layer undergoes martensitic transformation after the core, and compressive stress is formed on the surface, which improves the wear resistance and rolling contact fatigue performance [19].

At present, carburizing technology is mainly used in low-carbon steel or low-alloy steel, which has obvious effect on improving the strength of steel. However, there are few related studies on high carbon steel. In this study, the M50 steel was short-time carburized with different carbon potential, and its effect on the microstructure and the mechanical properties of the steel were studied.

2 Materials and Methods

The material used in this study is M50 steel, whose chemical composition is shown in Table 1. The test steel was obtained by vacuum smelting + vacuum consumable smelting, and rolled to obtain bars with diameters of 16 and 10 mm. The bars were processed into cylindrical samples with the dimension of $\Phi12 \times 10$ mm for microstructure observation. The samples for impact and rotational bending fatigue tests were machined with the bars of $\Phi16$ mm and $\Phi10$ mm respectively, and the axis direction of the samples was the same as the rolling direction of the bars.

The carburizing, austempering, and tempering processes used in this study are shown in Fig. 1. The samples to be carburized were placed in a gas-shielded furnace and heated to 840, 1020 and 1090 °C in turn, and the holding time was 30, 15 and 12 min respectively. From the beginning of the heat preservation at 840 °C to the end at 1090 °C, the carburizing treatment was carried out in the gas shielded furnace with the fixed carbon potential, and the carbon potential was 0.6 and 0.8%, respectively. For comparative experiments, samples that did not require carburization were also subjected to the exact same heat treatment as the carburized samples in a high-temperature furnace (without carbon potential). After the carburized and uncarburized samples were kept at 1090 °C, they were directly put into a 200 °C salt bath furnace for austempering for 2 h, and then air-cooled to the room temperature. The quenched samples were tempered 3 times at 550 °C for 2.5 h. For the convenience of expression, UN-C is used in this paper to represent the uncarburized M50 steel, and Cp0.6 and Cp0.8 represent the carburized M50 steel with the carbon potential of 0.6% and 0.8%, respectively.

Table 1 Chemical composition of M50 bearing steel (wt%)

C	Cr	Mo	V	Mn	Si	Fe
0. 8	4. 02	4.05	0. 93	0. 29	0. 16	Bal

Fig.1 Heat treatment process
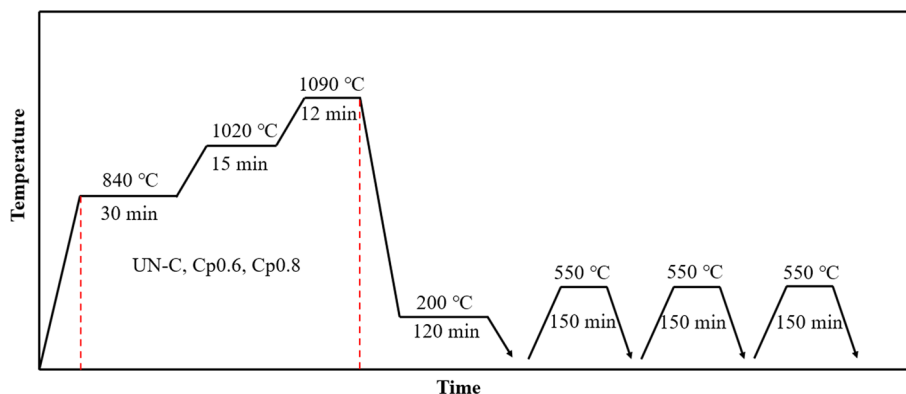
The XRD-7000S/L X-ray diffraction analyzer (XRD) and energy dispersive spectrometer (EDS) were used to analyze the phase of the samples. Then the samples were polished with 600–2000# sandpaper and polished, and then corroded with the etchant of 100 ml $C_2H_5OH + 5$ ml $HCl + 2.5$ g $C_6H_2OH(NO_2)_3$. The ZEISS Merlin scanning electron microscope (SEM) was used to observe the microstructure of the samples. The JEM-2100 transmission electron microscope (TEM) was used to the further observation of the microstructure, and the samples were prepared as the followings. The samples were first ground to 0.05 mm, and then double spray thinning was performed under the conditions of − 20 °C and voltage of 25 V. The used electrolyte was 10% $HClO_4 + 90\%$ C_2H_5OH, and the cooling medium was liquid nitrogen.

HVS-1000 Vickers hardness tester was used to test the hardness of the samples, the load was 500 g, and the

holding time was 15 s. The QBWP-10000 cantilever beam rotating bending tester was used to determine rotating bending fatigue limit. The standard samples used are shown in Fig. 2a. ZBC2302 Charpy impact test method was used to measure the impact energy of samples, and the fracture of the samples was observed by SEM. The dimensions of the used impact samples were shown in Fig. 2b.

3 Results

3.1 Microstructure

Figure 3 shows the quenched microstructure of the surface layer and the core of M50 steel prepared with different carbon potentials. Figures 3a-c show the microstructure of the surface layer of UN-C, Cp0.6, and Cp0.8 after austempering,

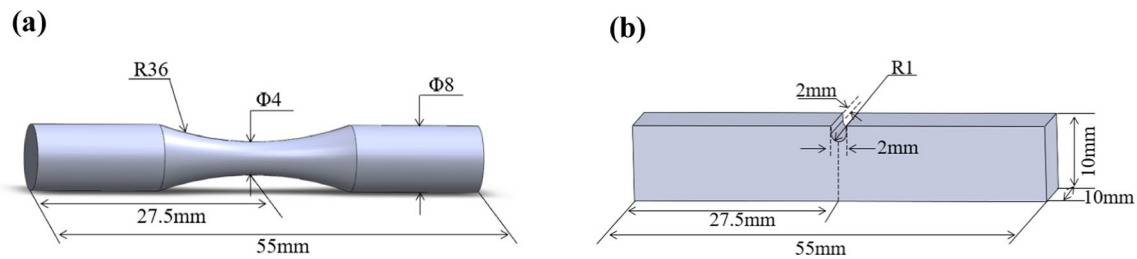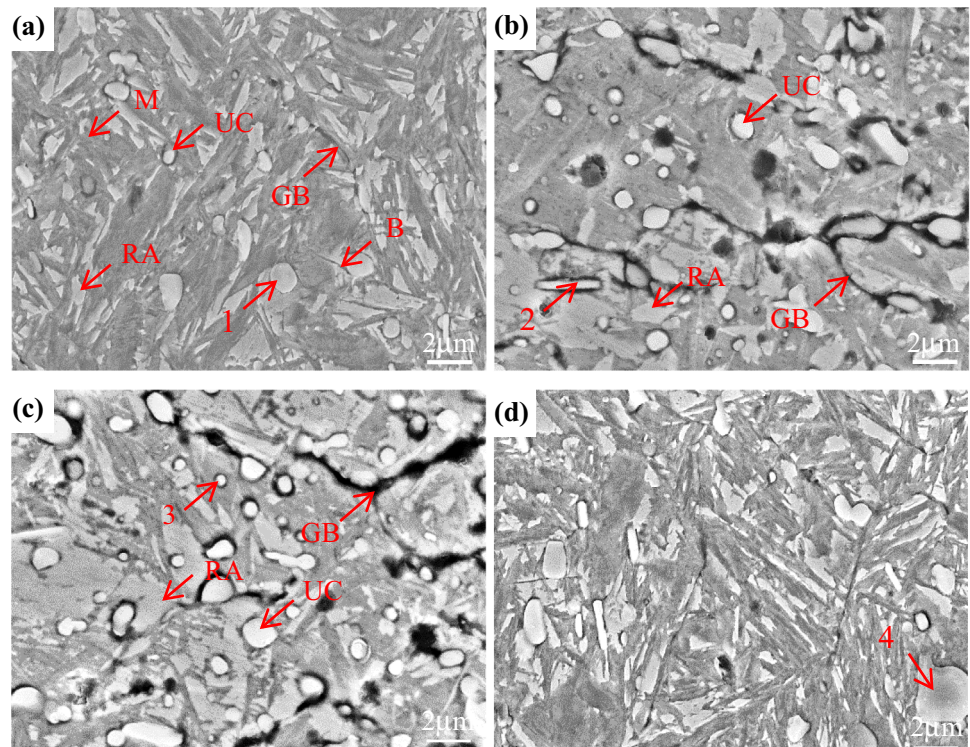**Fig. 2** The standard specimens for mechanical property tests **a** rotating bending fatigue test **b** Charpy impact test

Fig. 3 Microstructure of M50 steel after austempering **a** surface layer of UN-C **b** surface layer of Cp0.6 **c** surface layer of Cp0.8 **d** core region of Cp0.6

which is mainly composed of lath martensite (M), acicular bainite (B), blocky residual austenite (RA) and undissolved carbides (UC), but the number of them is different under different carbon potential conditions. There is a amount of martensite and bainite in the surface layer of UN-C, but a small amount of residual austenite and undissolved carbides, as shown in Fig. 3a. When the carbon potential is 0.6%, the content of martensite and bainite is significantly reduced. At the same time, the number of residual austenite and undissolved carbides increases, and clear grain boundary (GB) characteristics appear, as shown in Fig. 3b. When the carbon potential further increases to 0.8%, the amount of undissolved carbide increases, and grain boundaries become coarser, as shown in Fig. 3c. Figure 3d shows the microstructure of the core region of Cp0.6 after austempering, where the carbon content is not increased. The microstructure is consistent with that of the surface layer of UN-C (Fig. 3a), and that of the core region of Cp0.8, which are all omitted in this paper.

Figure 4 shows the TEM microstructure of Cp0.6 after austempering. Figure 4a presents the surface microstructure of Cp0.6, indicating that a small number of carbides (C) are distributed on the martensitic lath (M). The core microstructure of Cp0.6 is shown in Fig. 4b, the lath martensite and bainite (B) in the microstructure are observed. Figure 4c is the enlarged view of the red box in Fig. 4b, where the twin martensite (TM) can be observed. The surface and core microstructure of Cp0.8 after austempering is similar to that of Cp0.6, which is omitted here.

Figure 5 shows the microstructure of the surface layer and core of the tempered M50 steel with different carbon potentials. Figure 5a shows the surface microstructure of UN-C, indicating that there are a large number of secondary carbides (SC) precipitated dispersedly, showing the filamentary shape, and some undissolved carbides (UC) are exhibited. Figure 5b shows the microstructure of the surface layer of Cp0.6. Compared with UN-C, the number of precipitated

secondary carbides is reduced obviously. The microstructure of the surface layer of Cp0.8 is shown in Fig. 5c. The precipitated secondary carbides are acicular with the size of about 2 ~ 4 μm, and there are more granular undissolved carbides and the size is larger. Figure 5d shows the core microstructure of Cp0.6 after tempering, which is similar to the surface layer of UN-C (Fig. 5a). The core microstructures of UN-C and Cp0.8 is omitted in this paper for they are almost the same as Fig. 5d.

Figure 6 is the EDS analysis of carbides with different morphologies in Figs. 3 and 5. The larger-sized spherical carbides (Fig. 3a, arrow 1) and short rod-like carbides (Fig. 3b, arrow 2) are rich in Fe and Mo elements, as shown in Fig. 6a, which is consistent with the compositional characteristics of M_6C-type carbides [20, 21]. The smaller-sized spherical carbides (Fig. 3c, arrow 3) are rich in V element, which is consistent with the compositional characteristics of MC-type carbides [20, 21], as shown in Fig. 6b. The larger massive carbides (Fig. 3d, arrows 4) are rich in Mo element and conformed to the compositional characteristics of M_2C-type carbides [20, 21], as shown in Fig. 6c. Figure 6d shows the composition information of the secondary carbides (SC, Fig. 5) precipitated after tempering. The content of Fe is relatively high, which is in line with the characteristics of Fe_3C-type carbides, and the literature [22] also proposes consistent analysis.

Figure 7a shows the content of undissolved carbides and secondary precipitated carbides in the surface layer of M50 steel under different carbon potential conditions. After austempering, the content of undissolved carbides (UC) in the surface layer is 3.31%, and that increases after carburizing treatment. The content of surface layer carbides is 8.19 and 10.12% in the steel with carbon potential of 0.6 and 0.8. Carburizing treatment also has an effect on the precipitation of secondary carbides (SC) after tempering. The content of secondary carbides on the surface of the UN-C is 33.03%, while with the increase of carbon
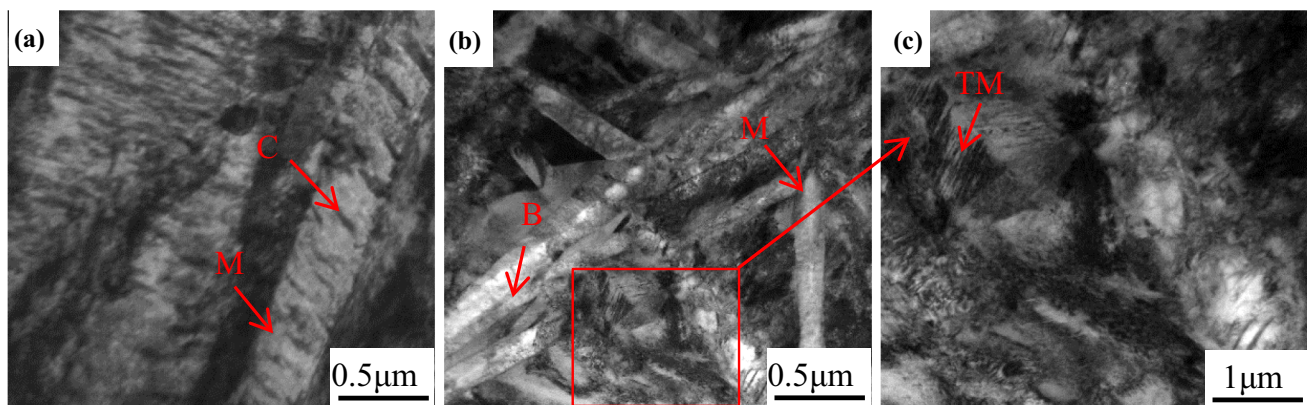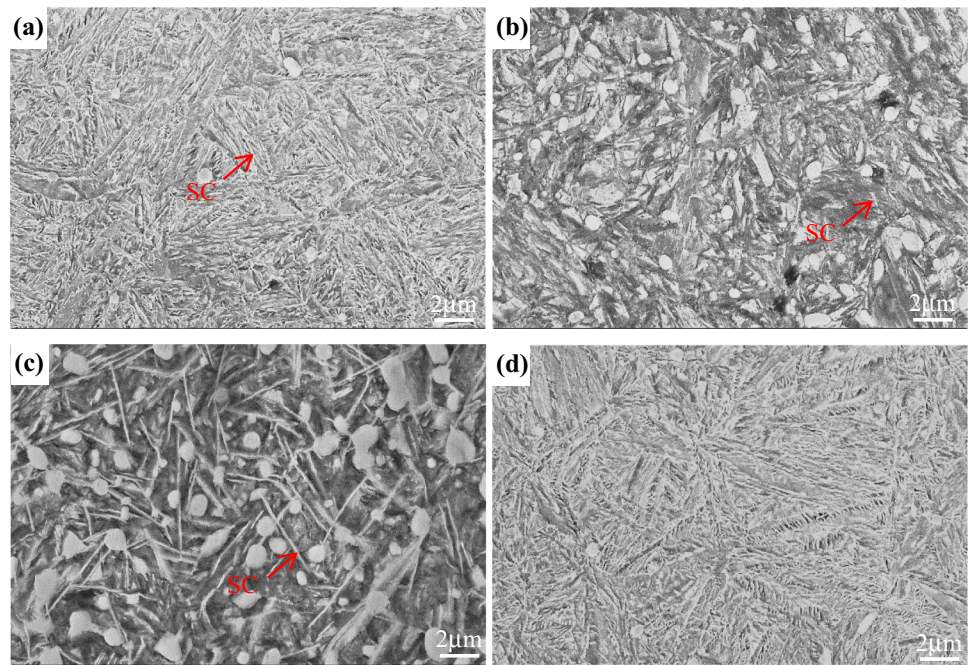

Fig. 4 TEM of Cp0.6 after austempering **a** surface layer of Cp0.6 **b**, **c** core region of Cp0.6

Fig. 5 Microstructure of M50 steel after austempering and tempering **a** surface layer of UN-C **b** surface layer of Cp0.6 **c** surface layer of Cp0.8 **d** core region of Cp0.6

potential, the content of secondary carbides is 15.72 and 20.62%. Figure 7b shows the sizes of undissolved carbides (UC) in the steel with different carbon potentials. With the increase of carbon potential, the mean size of UC are 0.52, 0.59 and 0.64 µm, respectively, and there exists a gradual increasing trend.

Figure 8 is the XRD pattern of the surfaces for the samples under different carbon potential conditions. Figure 8a shows the XRD pattern of the surface of the samples after austempering. The main diffraction peaks are α-Fe with the body-centered cubic structure and γ-Fe with the face-centered cubic structure, indicating the surface microstructure contains α-Fe and γ-Fe phases in all the samples with different carbon potential conditions. It is worth noting that under different carbon potential conditions, the number of different components after austempering is different. As the carbon potential increases from 0, 0.6 to 0.8%, the diffraction peak intensity of α-Fe gradually decreases, indicating qualitatively that the content of α-Fe gradually decreases, and the residual austenite content in the test steel was 29.94, 52.87 and 65.09%, respectively. While the diffraction peak intensity of γ-Fe (311) gradually increases, indicating the content of γ-Fe increases. From the enlarge view in Fig. 8a, the diffraction peak of γ-Fe (311) tends to shift to the low angle. According to the Bragg equation: $2d\sin\theta = n\lambda$, where d is the interplanar spacing, θ is the diffraction angle between the incident X-ray and the corresponding crystal plane, and λ is the X-ray wavelength and n is the diffraction order. As the diffraction angle θ decreases, the interplanar spacing d increases, indicating that the carbon content of γ-Fe increases.

Figure 8b is the XRD pattern of the surface of samples after tempering. The main diffraction peak is the α-Fe with body-centered cubic microstructure, and there is no obvious diffraction peak of γ-Fe, indicating that the content of γ-Fe is greatly reduced after tempering. As the carbon potential increases from 0 and 0.6 to 0.8%, the diffraction peak intensity of α-Fe gradually decreases, indicating that as the carbon potential increases, the amount of α-Fe is reduced.

3.2 Mechanical properties

Figure 9 shows the microhardness distribution of the tempered M50 steel with different carbon potential conditions. It can be seen that the core hardness of the samples is about 750 HV. Based on this hardness value, the depths of the carburized layers of Cp0.6 and Cp0.8 are about 0.98 and 1.18 mm respectively. The microhardness of UN-C remains stable from the surface to the core, which is about 750 HV. In the carburized area, the hardness of Cp0.6 and Cp0.8 reaches up to 807.7 HV and 813.4 HV respectively. As the distance from the surface increases, the hardness of Cp0.6 and Cp0.8 gradually decreases, and becomes stable finally. The value of hardness is mainly related to the change of carbon content [23].

Figure 10 shows the rotating bending fatigue strength of M50 steel with different carbon potential conditions. The test stipulates that when the number of cycles reaches 1×10^7 without breaking, it is considered that the life of the sample under the load stress condition is infinite. From Fig. 10, it can be seen that the rotational bending fatigue strength of UN-C, Cp0.6 and Cp0.8 are 1100, 1210 and 1125 MPa
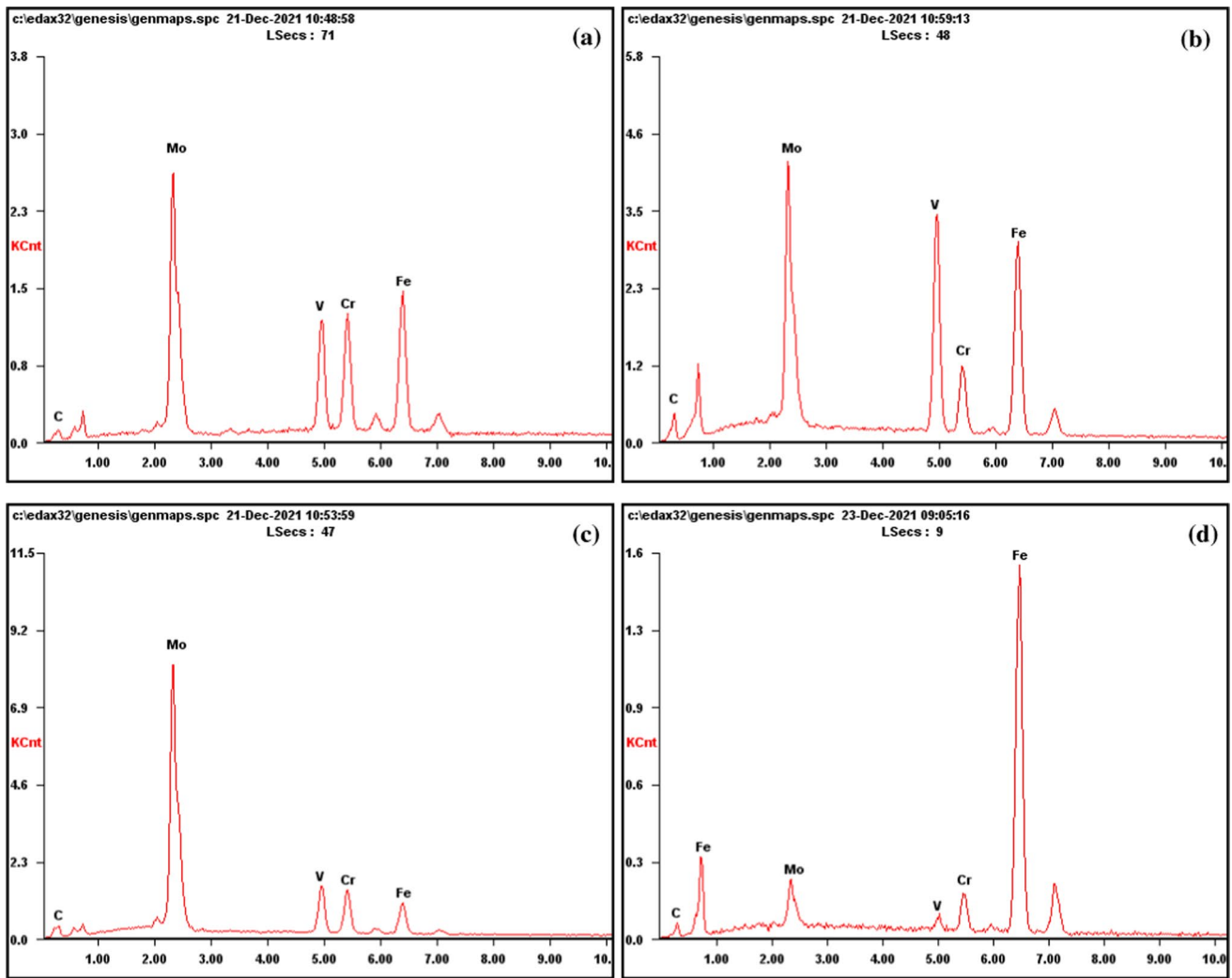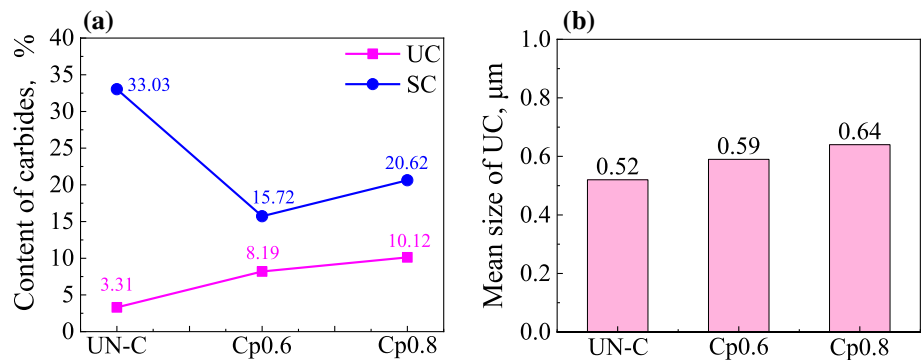
Fig. 6 EDS analysis of carbides **a** arrows 1, 2 in Figs. 3a, b **b** arrow 3 in Fig. 3c **c** arrow 4 in Fig. 3d **d** SC in Fig. 5c

Fig. 7 The content and size of carbides at the surface layer of M50 steel under different carbon potential conditions **a** Content of carbides **b** Size of UC (UC: undissolved carbide after austempering, SC: secondary precipitation carbide after tempering)

respectively, and the rotational bending fatigue strength of Cp0.6 is the highest.

Figure 11 shows the impact absorption energy of M50 steel with different carbon potential. It can be seen that the impact absorption energy of UN-C is 15.46 J, and that

of Cp0.6 is the highest at 16.72 J. As the carbon potential increases, the impact absorption energy of Cp0.8 decreases to 13.65 J.

Figure 12 shows the impact fracture morphology of M50 steel after short-term carburization with different

Fig. 8 XRD pattern of surface layer of M50 steel samples with different carbon potentials **a** after austempering **b** after tempering
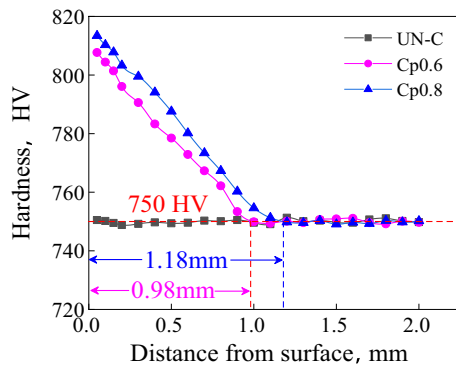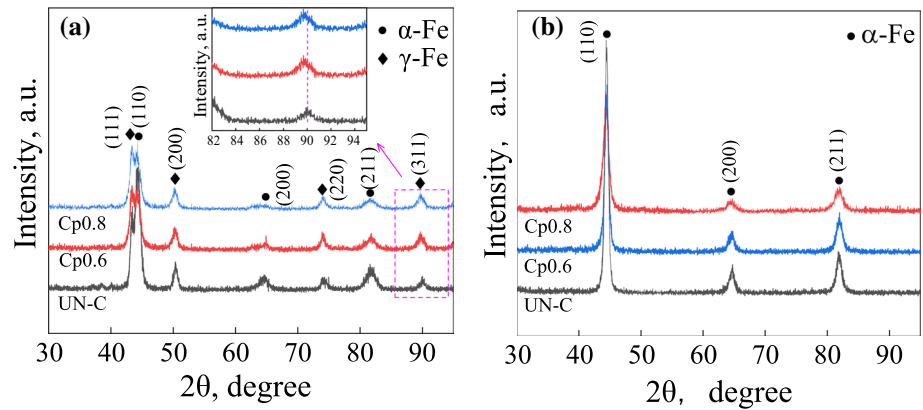

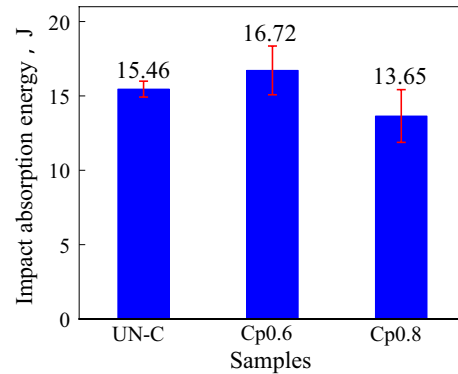**Fig. 9** Microhardness of M50 steel after austempering and tempering

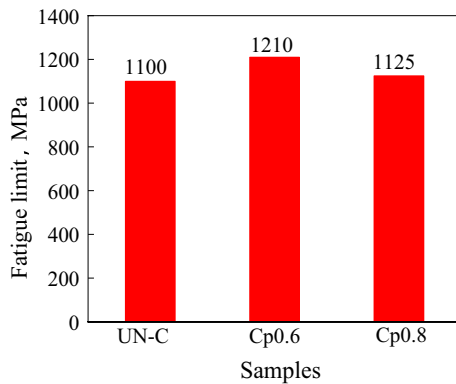**Fig. 11** Impact absorption energy of M50 steel samples with different carbon potentials

Fig. 10 Rotating bending fatigue limit of M50 steel with different carbon potentials

4 Discussion

4.1 Effect of Short-time Carburizing on the Microstructure of M50 Steel

From Figs. 3d-f, it can be seen there is no difference in the core structure of the austempered samples under different carbon potential conditions, and it is the same as the surface microstructure of UN-C, indicating that the short-term carburization mainly affects the surface microstructure of the steel. Figures 13a, c and e are the schematic diagrams of the surface microstructures of the quenched UN-C, Cp0.6 and Cp0.8 respectively, corresponding to the microstructure characteristics of Figs. 3a-c. It can be seen that the surface microstructure of UN-C is composed of lath martensite, acicular bainite, a small amount of retained austenite and undissolved carbides, and the grain boundary characteristics are not obvious, as shown in Fig. 13a. According to Figs. 13c and e, corresponding to the carbon potential of 0.6% and 0.8% respectively, the content of bainite and martensite formed in the surface microstructure decreases, while the amount of residual
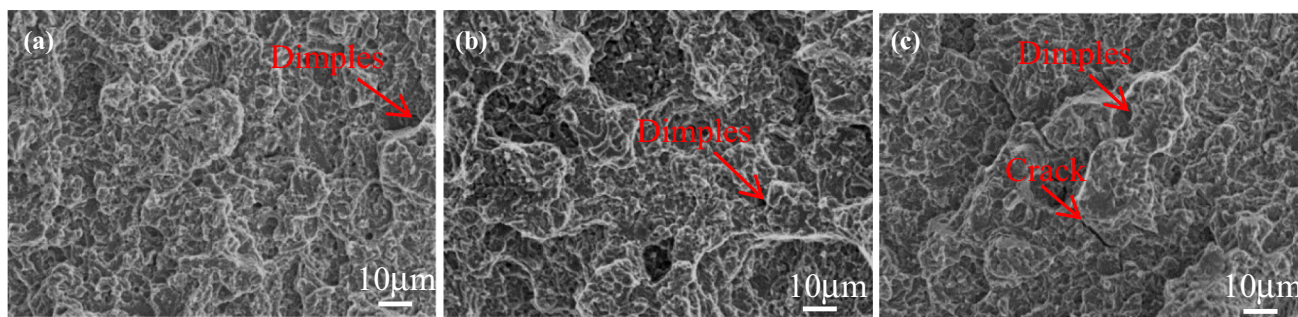
carbon potentials. It can be seen that the three fracture modes are typical ductile fractures. Some dimples are distributed in UN-C and Cp0.6, and the density is comparable, while there are some microcracks appear in Cp0.8.

Fig. 12 Impact fracture morphology of M50 steel samples with different carbon potentials **a** UN-C **b** Cp0.6 **c** Cp0.8

Fig. 13 Schematic diagram of microstructure evolution of M50 steel during austempering and tempering
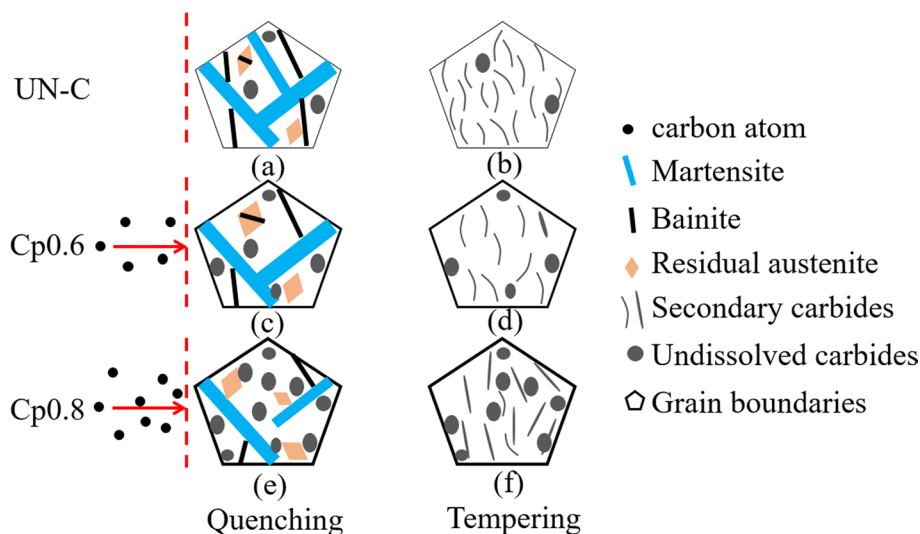
austenite increases, which is closely related to the carbon content in the austenite [24–26], as shown in Fig. 8a. With the increase of carbon potential, the carbon content of the carburized surface layer increases, where the stability of the austenite also increases, which makes the austenite in the surface layer difficult to transform into martensite and bainite. In addition, the number of undissolved carbides in the surface layer after austempering increases significantly with the increase of carbon potential, which is related to the fact that with the increase of carbon concentration, it is easier for carbon atoms to combine with strong carbide elements such as Cr and Mo during the austenitization process. The atomic arrangement at grain boundaries is disordered, and the carbon content increases with the enhancement of the carbon potential. Carbon atoms and alloying elements diffuse through grain boundaries and element accumulation occurs at the grain boundaries, which results in the gradual coarsening of the grain boundary after austempering.

Figures 13b, d and f are the schematic diagrams of the surface microstructures of the tempered UN-C, Cp0.6 and Cp0.8 respectively, corresponding to the microstructure characteristics of Figs. 5a-c. According to Fig. 13b, there are a large number of dispersedly precipitated secondary carbides with small size on the surface layer of UN-C. However, the surface microstructures of Cp0.6 and Cp0.8 after tempering are completely different from that of UN-C, as shown in Figs. 11d and f. There are small secondary carbides precipitated on the surface layer of Cp0.6, and a few acicular carbides appear at the same time. The surface microstructure of Cp0.8 is dominated by larger acicular carbides, which are basically arranged parallelly. According to the literature [27], the coarse austenite grain and high carbon content can cause the precipitation of acicular carbides with large size, which is mainly affected by diffusion conditions. When the acicular carbides are formed, a relatively wide region on both sides of the carbides becomes to be carbon-poor zone of residual austenite, and thus the thickness of acicular carbides is limited. However, at both ends of the needle, as it continues to extend into the carbon-rich residual austenite and the carbon supplementation can be obtained, the acicular carbides are formed finally.

4.2 Effect of Short-time Carburizing on Mechanical Properties of M50 Steel

It can be seen from Fig. 10 that the rotational bending fatigue limits of Cp0.6 and Cp0.8 are higher than those of UN-C. After short-term carburizing, the Ms point of the surface layer of M50 steel decreases. During the austempering process, martensitic transformation occurs in the core first and then in the surface layer, which results in the certain residual compressive stress in the surface layer, and this has a certain inhibitory effect on the propagation of fatigue cracks [28, 29]. In addition, residual austenite also has certain influence on fatigue strength, which has the following two aspects. On one hand, residual austenite in the surface layer reduces the compressive stress that is beneficial to the bending fatigue strength. It can be seen from Fig. 8a that the amount of residual austenite in the surface layer gradually increases after austempering, and the surface compressive stress resulted from the martensite transformation decreases. On the other hand, the propagation of fatigue cracks in austenite absorbs more energy than in martensite, which has a certain hindering effect on crack propagation and is beneficial to improve fatigue strength. Moreover, some residual austenite transforms into martensite in the process of rotating bending fatigue cycle, which is superior to the martensite formed during heat treatment in improving the performance [30].

Figure 3 shows that the number of the undissolved carbides in the surface layer after austempering increases with the increase of carbon potential. These carbides are larger in size, which is detrimental to the rotational bending fatigue performance, and are likely to be the source of cracks. From Fig. 5, it can be seen that the content of carbides in the surface layer after tempering increases with the increase of carbon potential and the size of carbides increases, especially the acicular carbides with $2 \sim 4$ μm length appearing in the surface layer of Cp0.8, which leads to the lower rotational bending fatigue limit compared to that of Cp0.6. The larger carbides also increase the brittleness of the material and reduce the toughness, and cracks are observed in the fracture morphology of Fig. 12c.

Some studies have found that toughness is not determined by a single brittle microstructure, that is, not only by a weak microstructure that is prone to fracture, but by a mixed mechanism of multiple microstructures interacting with each other [31]. As shown in Fig. 8b, the surface martensite content of UN-C is the highest, followed by Cp0.6, and that in Cp0.8 is the lowest. When the steel is subjected to impact load, cracks propagate from the martensite first. The more the martensite content is, the easier the crack propagation is, and the lower the required propagation energy is, so the toughness of UN-C is lower than that of Cp0.6. The blocky residual austenite in the surface layer of Cp0.8 after austempering is the most, as shown in Figs. 3a and 8a. Even if

the residual austenite decreases after tempering, the residual austenite under tempering is still blocky, showing inferior mechanical stability and thermal stability. Martensitic transformation is easy to occur under impact load, which brings harmful effects on the toughness of the steel, increases the brittleness of material, and leads to the decrease of impact toughness. Therefore, the toughness of Cp0.8 is the worst.

5 Conclusions

(1) After short-term carburizing treatment of M50 steel, with the increase of carbon potential, the number of residual austenite and undissolved carbides increases after austempering, and the characteristics of grain boundaries appear gradually clear. After tempering, the length of the acicular carbides of Cp0.8 is $2 \sim 4$ μm.

(2) The rotational bending fatigue limit of M50 steel increases after short-time carburizing treatment. When the carbon potential is 0.6%, the rotating bending fatigue limit of M50 steel is the highest, which is 1210 MPa. When the carbon potential is 0.8%, the increase of acicular carbides reduces the rotating bending fatigue limit of M50 steel.

(3) When the carbon potential is 0.6%, the impact absorption energy of M50 steel is the highest to be 16.72 J. When the carbon potential increases to 0.8%, the impact absorption energy of M50 steel reaches the lowest to be 13.65 J. When the carbon potential is 0.6%, M50 steel has good comprehensive mechanical properties.

Declarations

References

1. H.K.D.H. Bhadeshia, J.W. Christian, Metall. Mater. Trans. A **21**, 767 (1990)
2. F. Wang, D. Qian, H. Mao, Y. He, B. Shu, J. Mater. Res. Technol. **9**, 6712 (2020)
3. W. Liu, Y. Cao, Y. Guo, M. Sun, B. Xu, D. Li, J. Mater. Sci. Technol. **38**, 170 (2020)
4. Y.H. Wei, X.F. Yu, Y. Su, X.Y. Shen, Y.Z. Xia, W.W. Yang, J. Mater. Res. Technol. **10**, 651 (2021)
5. J. Zhao, X. Zhao, X. Zhao, C. Dong, S. Kang, Mater. Sci. Eng. A **744**, 86 (2019)
6. W. Gong, Y. Tomota, S. Harjo, Y.H. Su, K. Aizawa, Acta Mater. **85**, 243 (2015)
7. X.H. Lu, D.S. Qian, W. Li, X.J. Jin, Mater. Lett. **234**, 5 (2019)

8. M. Ueda, K. Matsuda, Wear **444–445**, 203120 (2020)
9. J.K. Xiao, H. Tan, J. Chen, A. Martini, C. Zhang, J. Alloy. Compd. **847**, 156533 (2020)
10. Y. Chen, F. Mei, X. Lin, H. Zhang, J. Gao, T. Yuan, R. Li, T. Peng, Thin Solid Films **713**, 138344 (2020)
11. Y. Peng, Z. Liu, C. Chen, J. Gong, M.A.J. Somers, Mater. Sci. Eng. A **769**, 138524 (2020)
12. Z. Liu, S. Wang, Y. Feng, Y. Peng, J. Gong, M.A.J. Somers, Int. J. Fatigue **159**, 106837 (2022)
13. P. Juijerm, I. Altenberger, Scripta Mater. **55**, 1111 (2006)
14. F. Rotundo, L. Ceschini, C. Martini, R. Montanari, A. Varone, Surf. Coat. Tech. **258**, 772 (2014)
15. S. Fudger, D. Sediako, P. Karandikar, C. Ni, Mater. Sci. Eng. A **699**, 10 (2017)
16. S. Qin, C. Zhang, B. Zhang, H. Ma, M. Zhao, J. Mater. Sci. Technol. **16**, 1136 (2022)
17. S. Su, L. Wang, R. Song, Y. Wang, J. Li, C. Chen, Mater. Lett. **280**, 128486 (2020)
18. B.Z. Li, C.S. Li, Z.X. Li, J.B. Dong, Procedia Manuf. **15**, 1612 (2018)
19. J.P. Su, J. Harbin Bearing **32**, 12 (2011)
20. B. Decaudin, C. Djega-Mariadassou, G. Cizeron, J. Alloy. Compd. **226**, 208 (1995)
21. J.E. Bridge, G.N. Maniar, T.V. Philip, Metall. Mater. Trans. B **2**, 2209 (1971)
22. F. Wang, D. Qian, L. Hua, H. Mao, L. Xie, X. Song, Z. Dong, Mater. Sci. Eng. A **771**, 138623 (2020)
23. L. Ma, M.Q. Wang, J. Shi, W.J. Hui, H. Dong, Mater. Sci. Eng. A **498**, 258 (2008)
24. T. Sourmail, M. Millot-Méheux, Mater. Sci. Technol. **32**, 1126 (2016)
25. S. Lee, S.-J. Lee, B.C. De Cooman, Scripta Mater. **65**, 225 (2011)
26. J. Hidalgo, K.O. Findley, M.J. Santofimia, Mater. Sci. Eng. A **690**, 337 (2017)
27. C.W. Xuan, Y.C. Wang, L.B. Zhang, Jinshu Rechuli/Heat Treat. Met. **1990**(1), 20 (1990)
28. Y. Zhang, L.C. Lu, G.T. Xu, G. Wang, M.H. Zhao, Eng. Fail. Anal. **131**, 105839 (2022)
29. Z. Cao, T. Liu, F. Yu, W. Cao, X. Zhang, Y. Weng, Int. J. Fatigue **131**, 105351 (2020)
30. B. Su, H. Zhao, R. Xiao, M. Huang, Q. Sun, M. Zhang, Hot Working Technology **46**, 22 (2022)
31. L. Zhou, G. Tang, X. Ma, Y. Shi, T. Wu, F. Ma, K. Zhao, Jinshu Rechuli/Heat Treat. Met. **43**(7), 144 (2018)